ACS APPLIED MATERIALS & INTERFACES

Research Article

www.acsami.org

Transparent Conducting Aerogels of Antimony-Doped Tin Oxide

Juan Pablo Correa Baena[†,‡] and Alexander G. Agrios*[,†,‡]

[†]Civil and Environmental Engineering and [‡]Center for Clean Energy Engineering, University of Connecticut, Storrs, Connecticut 06269, United States

ABSTRACT: Bulk antimony-doped tin oxide aerogels are prepared by epoxide-initiated sol–gel processing. Tin and antimony precursors are dissolved in ethanol and water, respectively, and propylene oxide is added to cause rapid gelation of the sol, which is then dried supercritically. The Sb:Sn precursor mole ratio is varied from 0 to 30% to optimize the material conductivity and absorbance. The materials are characterized by electron microscopy, transmission electron microscopy, X-ray diffraction, X-ray photoelectron spectroscopy (XPS), nitrogen physisorption analysis, a four-point probe resistivity measurement, and UV–vis diffuse reflectance spectroscopy. The samples possess morphology typical of aerogels without significant change with the amount of doping. Calcination at 450 °C produces a cassiterite crystal structure in all aerogel samples. Introduction of Sb at 15% in the precursor (7.6% Sb by XPS) yields a resistivity more than 3 orders of magnitude lower than an undoped SnO_2 aerogel. Calcination at 800 °C reduces the resistivity by an additional 2 orders of magnitude to 30 Ω·cm, but results in a significant decrease in surface area and pore volume.

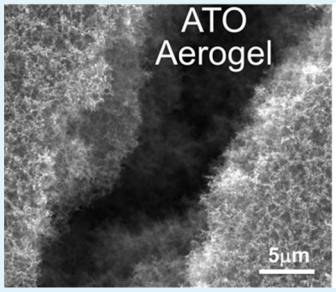

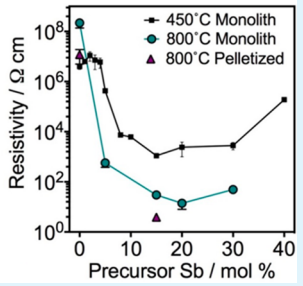

KEYWORDS: *antimony-doped tin oxide, transparent conducting oxides, aerogels, porous electrodes*

1. INTRODUCTION

Tin oxide materials are commonly doped with fluorine (FTO) or antimony (ATO) or dissolved in indium oxide (ITO) to make transparent conducting oxides (TCO). The high cost of indium is disadvantageous for ITO and has led many researchers to shift attention to low-cost alternatives such as FTO and ATO. In the former, fluorine atoms replace oxygen atoms in the lattice, and in the latter, antimony replaces tin, in either case resulting in a highly doped semiconductor. Under optimized conditions, TCO materials can exhibit high Hall mobility, low resistivity, and high transmittance in the visible range, even from low-temperature synthesis.[1] These properties make TCOs essential in a wide variety of applications such as solar energy conversion,[1−3] water splitting,[4] optoelectronic devices,[5] and gas sensors.[6] These have traditionally been processed as compact films[7−10] exhibiting high conductivities. Although achieving high doping levels in nanoparticles by wet-chemical synthesis is challenging,[11] nanoparticles of FTO[12] and ATO[13,14] have been realized from solution. Mesoporous films of such nanoparticles have been made by block copolymer templating[15−17] or by simple doctor blading.[14] Nanoparticle systems are significantly less conductive than their compact film counterparts due to grain boundary scattering, which limits their electron mobilities.[9] However, the morphologies that such sols can produce are desirable for applications that require a high surface area for contact between the TCO[18] and another phase, such as core–shell architectures in nanostructured solar cells[2] and water splitting devices.[19]

Aerogels are 3D monolithic structures composed of networked nanoparticles and exhibit high surface area, high porosity, and good particle interconnectivity.[20] These are processed as sol–gels where a catalyst causes the gelation of the sol, commonly at low temperatures. Acid- and base-catalyzed formations of silica aerogels have long been widely studied.[21,22] More recently, Gash and co-workers developed an epoxide-initiated sol–gel process used to synthesize iron oxide aerogels.[23] The hydrated metal is deprotonated by the epoxide, which links it with other hydrated metals via olation and oxolation to form metal oxide particles. These in turn cross-link to form a 3D array of particles, i.e., a gel. This sol–gel process has been used to make other materials such as ZnO[24] and SnO_2 aerogels.[25] Its main advantage is that the wet gels can be prepared from many metal salts that are low cost and easy to handle.

Silica aerogels have been used in dye-sensitized solar cells (DSCs) as mesoporous templates for TiO_2[26] and ZnO[27] coatings. Given the insulating nature of silica, electrons are transported by the thin semiconducting shells. A transparent conducting oxide would be a preferable aerogel material as it could provide charge collection in addition to the favorable mesoporous structure. Previously,[28] we cast ATO aerogels as thin films and prepared DSCs by coating the mesoporous nanostructure with TiO_2 by atomic layer deposition and demonstrated improved performance in the presence of an electron shuttle with fast recombination, indicating advantageous electron collection by the conducting aerogel.

Received: July 31, 2014
Accepted: October 8, 2014
Published: October 8, 2014

 © 2014 American Chemical Society

Here, we report the synthesis and detailed characterization of TCO aerogels in bulk form by supercritical drying of ATO gels. We have used the epoxide-assisted method to form gels with varying concentrations of Sb. We used scanning electron microscopy (SEM), X-ray photoelectron spectroscopy (XPS), and electrical conductivity measurements (among others) to study the effects of Sb doping on the morphological, optical, and electronic properties of SnO_2 aerogels.

2. EXPERIMENTAL SECTION

2.1. Synthesis and Preparation of Doped and Undoped Aerogels. All chemicals were purchased from Sigma-Aldrich and were ACS grade or better. In a typical procedure, $SnCl_4{\cdot}5H_2O$ (0.6 M) is dissolved in absolute ethanol (or other solvent) and NH_4F (7 M, mostly used at a 1:1 of F:Sn precursor) in water.[29] The tin solution is placed in a water bath at 60 °C for 5 h and the fluoride solution is added to it dropwise. A white precipitate forms but redissolves after about 2 h. $SbCl_5$ is dissolved in HCl (37%) at 2 M. The antimony is admixed in the solution at different mole ratios labeled as x% Sb, where x = [Sb]/[Sn], ranging from 0 to 30%.

In a common procedure, propylene oxide (PPO) is added (in two aliquots to avoid boiling over the synthesis solution due to rapid heat generation in the reaction) to the solution in an ice bath at a PPO:Sn ratio of 11:1.[23] The gelation occurs in 150 s after PPO addition, and the solution changes from a clear sol to a semitransparent white gel. The reaction is allowed to proceed for 20 min in a capped vial, which is subsequently filled with ethanol to age for 24 h. The solvent and byproducts are then washed with acetone three times over 3 days. The gels are transferred to a custom-built pressure vessel that is filled with liquid CO_2. The acetone is washed out by the liquid CO_2 over the course of 3 days and the vessel is heated above the critical point of the CO_2 (32 °C, 7.38 MPa). The temperature and pressure are held constant at about 45 °C and 9 MPa, respectively, for 60 min and then depressurized over 180 min to room temperature and pressure. The samples are then calcined at 450 °C in air for 30 min after heating at a rate of 3 °C/min.

2.2. Characterization. SEM (FEI Quanta FEG250 SEM in high vacuum mode) was used to study the morphology of the aerogels and transmission electron microscopy (TEM, FEI Tecnai T12 S operated at 120 kV accelerating voltage) to study particle shape and size. The samples were analyzed by XRD using a Bruker D8 Advance X-ray diffractometer using Cu Kα radiation (λ = 0.154 178 nm) at a scanning rate of 0.02° s^{-1} in the 2θ range from 20° to 60°. The crystallite size of the SnO_2 materials was determined by the Scherrer equation[30] $D = (0.9\lambda)/(\beta \cos \theta)$, where D is the crystallite size, λ is the X-ray wavelength, β is the full width at half-maximum (fwhm), and θ is half of the angle of diffraction. Elemental composition was determined by X-ray photoelectron spectroscopy (XPS) with a PHI 595 multiprobe system using an aluminum anode system with Kα = 1486.6 eV. Ground aerogel samples were placed and analyzed on a double-sided carbon tape. The spectra were corrected for sample charging effects using the C 1s peak at 284.6 eV. A Micromeritics ASAP 2020 accelerated surface area and porosimetry analyzer was used to determine the Brunauer–Emmett–Teller (BET) specific surface area, Barrett–Joyner–Halenda (BJH) pore volume, and size of the doped and undoped aerogels. The aerogel monolith resistivity (ρ) was determined by the common method of four-point probe technique.[31] Tungsten needles were placed atop the monolithic aerogel disks (1.2 cm diameter by 1 cm in height) and room temperature resistance was obtained from low voltage IV curves (−0.5 to +0.5 V) through the aerogel structure using the formula $\rho = 2\pi sF\ (V/I)$, where s is the spacing of the probes (0.6 mm), F is the correction factor dependent on sample geometry (taken as unity due to the large size of samples compared to the probe spacing), and V/I was extracted from the probe measurements. Diffuse reflectance measurements of aerogel powders diluted 10 times in barium sulfate were made using a Shimadzu UV-2450 UV–vis spectrometer with an IRS-2200 integrating sphere. Data were plotted as the Kubelka–Munk transform versus wavelength using the function $F(R) = (1 - R)^2/2R$, where R is the observed reflectance.

3. RESULTS AND DISCUSSION

3.1. Synthesis. Several solvents were investigated in the sol–gel process to produce monolithic gels. Table 1 presents the solvents, the ratio of the F to Sn in the precursor solution, whether it dissolves and gels, and the time required to gel (t_{gel}). The tin salt dissolved readily in all solvents when no fluorine was present. Precipitates were formed as NH_4F was added to the solution, but for samples marked "yes" in the "clear solution" column in Table 1, the precipitates redissolved after 2 h of stirring in a 60 °C water bath. Up to a F:Sn atom ratio of 1.25:1, ethanol was able to effectively dissolve the salts, but white precipitates formed above that ratio. Gel formation was observed for all 0:1 samples, regardless of the solvent. These yielded translucent gels with an initial firm bounce, but shrank in the capped vial after 30 min of PPO addition. To avoid the evaporation of the solvent and prevent the aforementioned shrinkage, the gel's original solvent was added to the vial 20 min after the PPO addition and the vial was capped. Ethanol was selected as the solvent for the remainder of this study based on its ability to dissolve a wide range of precursor compositions and result in gel formation.

Table 1. Summary of Solvent and NH_4F Effect on Solutions and Gelation of SnO_2 (0.6M $SnCl_4$, H_2O/Sn = 13, PPO/Sn = 11)

solvent	precursor F:Sn	clear solution	gel formation	t_{gel} (min)
methanol	0:1	yes	yes	50
	0.5:1	yes	no	
	1:1	no	no	
ethanol	0:1	yes	yes	12
	0.5:1	yes	yes	7
	1:1	yes	yes	2.5
propanol	0:1	yes	yes	13
	0.5:1	yes	yes	2.5
	1:1	no	no	
butanol	0:1	yes	yes	13
	0.5:1	no	no	
	1:1	no	no	
acetonitrile	0:1	yes	yes	13
	0.5:1	no	no	
	1:1	no	no	
dimethylformamide (DMF)	0:1	yes	yes	20
	0.5:1	no	no	
	1:1	no	no	

Fluoride is commonly used as a catalytic agent in silica sol–gel processing, and affects its gel times[32] and physical properties.[33] The addition of F has also been found to decrease the shrinkage in silica gels and aerogels.[22] We found that gels with no fluorine content tended to shrink during the aging and supercritical drying (SCD) processes, and show severe shrinkage after calcination at 450 °C. In contrast, gels with higher fluorine content experienced little gel shrinkage after PPO addition during aging, SCD, and calcination. For these reasons, fluorine-containing gels proved vital to achieving aerogel monolithic thin films without cracks or delamination

(Figure 1, bottom). However, resistivity was not significantly changed by the use of NH_4F in the reaction. For aerogels made

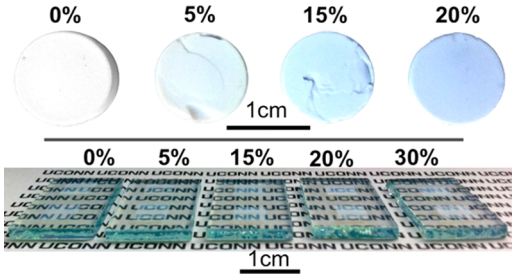

Figure 1. Photographs of SnO_2 cylindrical aerogel monolith (top) and thin films on glass (bottom) at different Sb/Sn precursor mole ratios after calcination at 450 °C for 30 min.

with NH_4F, XPS analysis revealed only a small F 1s peak in the calcined samples. Ammonium fluoride therefore had a significant structural effect on the SnO_2 aerogel despite a lack of electronic effect. The effects of fluorine on the gel structure will be the subject of a future study. The basic approach selected for the aerogels described in the remainder of this paper was ethanol-based synthesis of SnO_2 aerogels with NH_4F included at a F:Sn ratio of 1:1 for the favorable resulting structure, while antimony was added as a dopant to render the aerogel electrically conducting. The aerogels were brittle but could be subjected to contact electrical measurements. They collapsed due to capillary forces when immersed in liquid, but we reported previously that thin-film forms of these materials are robust after coating by atomic layer deposition and can withstand wetting and drying.[28]

Bulk aerogels made as described above exhibited no visible shrinkage during SCD, although minor shrinkage was noticed after calcination at 450 °C for 30 min. The addition of Sb had no visible change in the bulk aerogel appearance except for a blue-gray color that appeared following calcination in materials doped with more than 5% Sb (Figure 1, top). Calcination at 800 °C induced further shrinkage of the aerogel monoliths and the blue color became more intense. This color has been attributed to the absorbance of electrons in the conduction band of the semiconductor.[34−36] Alternatively, it has been suggested that Sb^{5+} and Sb^{3+} create impurity levels at or below the conduction band of the semiconductor, effectively reducing its bandgap, which results in the blue coloration observed here.[37] The color change has been consistently observed in different synthetic processes using antimony as a dopant[13,36,38] and with the introduction of oxygen vacancies.[14] The aerogels were scattering in the bulk form but they were transparent when made as thin films, as is demonstrated in the bottom part of Figure 1 and detailed previously.[28]

3.2. Structure. SEM images of the undoped (Figure 2a) and doped (Figure 2b,c,d, respectively) aerogels calcined at 450 °C reveal the open pore structure and good particle interconnectivity characteristic of aerogel materials. At this magnification, all samples are qualitatively of the same morphology regardless of the Sb doping level. However, some quantitative differences were revealed by more detailed analyses. The results of nitrogen adsorption/desorption measurements are shown in Table 2.[39] The isotherms (Figure 3, top) were type IV with an H1 hysteresis, as reported for other SnO_2 aerogels.[25] The pore size distribution (Figure 3, bottom) showed that the materials are mesoporous, in

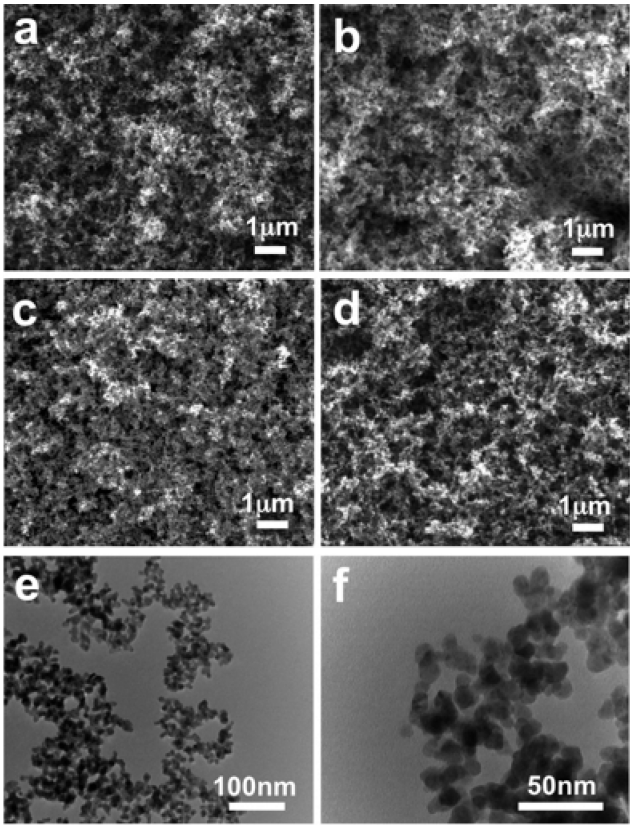

Figure 2. SEM images of SnO_2 aerogels undoped (a) and doped with 5 (b), 10 (c), and 15 (d) % Sb as the precursor Sb/Sn mole ratio. TEM images of undoped SnO_2 at different magnifications (e and f). All samples were calcined at 450 °C.

Table 2. Compositional Analysis and Physical and Electronic Properties of Doped and Undoped SnO_2 Aerogels

calcination conditions	precursor Sb/Sn (%)	XPS Sb/Sn (%)	BET surface area (m^2 g^{-1})	BJH pore volume (cm^3 g^{-1})	BJH mean pore radius (nm)
450 °C, 30 min	0		206	0.93	17
	5	3.1	169	0.68	14
	10	5.6	143	0.55	14
	15	7.6	103	0.42	16
	20	12.4	97	0.65	15
	30	13.2	98	0.43	19
800 °C, 6 h	0		14	0.05	13
	15	16.2	30	0.11	15
	30	21.6	38	0.17	18

agreement with the TEM images (Figure 2e,f), with a significant fraction of pores near the edge of the microporous range as has been observed in other metal oxide aerogels.[40] The pore distribution also shows pores in the macro region (up to about 140 nm), as can be seen in the SEM images (Figure 2).

ATO aerogels calcined at 450 °C exhibited high surface areas (100−200 m^2/g) in the range of other calcined metal oxide aerogels.[24,41] However, the addition of the Sb precursor up to 15% consistently decreased the surface areas and pore volumes of the aerogels. No significant change in BET surface area was seen from 15 to 30% Sb. Similarly, the pore volume saw no significant change from 15 to 30% Sb, although it showed an

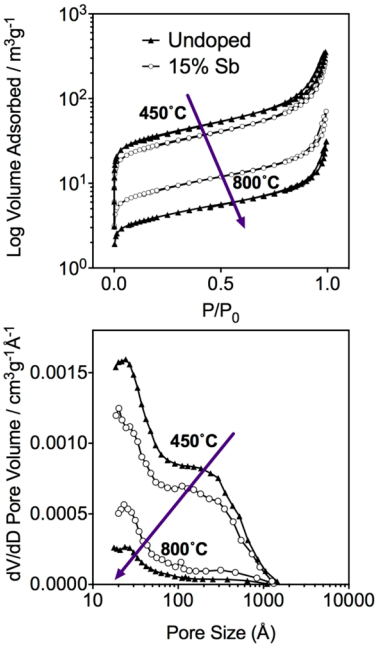

Figure 3. Nitrogen adsorption/desorption isotherms for undoped and 15% Sb-doped SnO_2 aerogels calcined at 450 and 800 °C (top) and their respective pore size distribution (bottom).

increase at 20%. The average pore radius showed no clear overall trend with dopant concentration.

Aerogels calcined at 800 °C for 6 h underwent visible monolith shrinkage and this was reflected in the nitrogen physisorption analysis (Figure 3). Comparing sintering at 450 °C for 30 min to 800 °C for 6 h, pore volume for undoped and 15% Sb-doped aerogels decreased (Table 2) from 0.93 and 0.42 $cm^3\ g^{-1}$ to 0.11 and 0.05 $cm^3\ g^{-1}$, respectively. The pore size distribution showed a pronounced decrease in the mesopore region with a higher volume of smaller pores (Figure 3, bottom). The BET surface area for 0 and 15% Sb decreased from 206 and 103 $m^2\ g^{-1}$ at 450 °C to 14.2 and 29.8 $m^2\ g^{-1}$ at 800 °C, respectively, which is indicative of particle growth and sintering.[42] These results align with those of Davis et al., who measured a surface area of 39 m^2/g and a pore volume of 0.16 $cm^3\ g^{-1}$ for ITO aerogels prepared by an epoxide-initiated process and calcined at 600 °C.[43]

XRD patterns of aerogel powders were obtained for undoped and doped samples (Figure 4, left). All samples matched the cassiterite pattern (JCPDS No. 41-1445) with (110), (101), (200), and (211) lattice planes. No peaks representing other phases were observed, suggesting that the antimony atoms were accommodated in the SnO_2 lattice. Undoped materials calcined at different temperatures were analyzed and found to be amorphous below 400 °C, with clear peaks emerging at and above 450 °C (data not shown). The introduction of Sb caused a broadening of the peaks suggesting a decrease in the particle size. The aerogels calcined at 800 °C exhibited much sharper peaks with evident improvement in crystallinity (Figure 4, left). At 450 °C, the (211) peak overlaps with a neighboring peak, whereas this phenomenon disappears at 800 °C. The Scherrer equation was used on the three main peaks of aerogels calcined at 450 and 800 °C to quantify the effect of doping and temperature on crystallite size. For samples calcined at the lower temperature, the (110) and (211) peaks show similar values: the crystallite size decreased from about 3.6 nm for

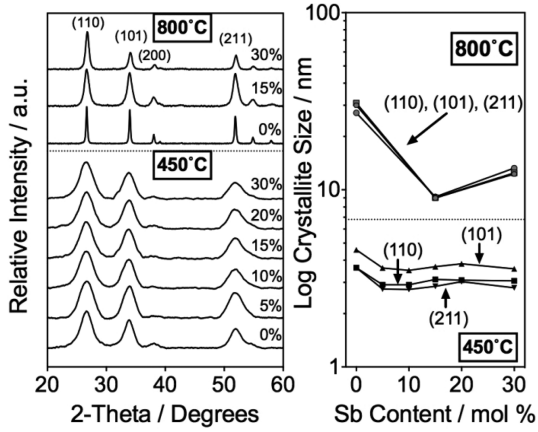

Figure 4. Effect of calcination temperature and Sb doping on crystal structure with XRD patterns of undoped and doped SnO_2 aerogels (left) and crystallite sizes (right) calculated with the Scherrer equation from the three main peaks, listed by precursor % Sb.

undoped samples to 2.9 nm for 30% Sb (Figure 4, right). The (101) peak gives the same trend with slightly elevated values. A negative effect of doping on crystallite size is consistent with other reports for doped metal oxide nanoparticles with similar synthetic processes.[36,44−47] Goebbert et al., for example, reported a similar trend for ATO nanoparticles prepared at 150 °C, where doping reduced the crystallite size from 7 to 3 nm.[48] These crystallite sizes are smaller than the particle size of ca. 10 nm observed by TEM images (Figure 2f), suggesting that the particles are polycrystalline. Notably, no significant shifts of peak positions were observed upon doping with Sb, indicating that the unit cell dimensions were not significantly changed despite the difference in ionic radius between 6-coordinate Sn^{4+} (0.69 Å) and Sb^{5+} (0.60 Å). Others have reported small or undetectable peak shifts resulting in minimal changes to unit cell parameters in Sb-doped SnO_2 films.[49,50] This may indicate that much of the Sb rests at grain boundaries or particle surfaces with smaller amounts taken into the crystal lattice; this will be examined in a future study.

Aerogels calcined at 800 °C saw a dramatic increase in the crystallite size (Figure 4, right). This was especially true for undoped samples, which yielded crystallites about 30 nm in size. Interestingly, the effect was not as marked for samples doped with 15 and 30% Sb, which produced crystallites of 9 and 12 nm, respectively. These results are consistent with the decrease in surface area of samples calcined at 800 °C (Table 2).

3.3. Sb Analysis. X-ray photoelectron spectroscopy (XPS) was conducted for aerogel samples with 0, 5, 10, 15, 20, and 30% Sb calcined at 450 °C (Figure 5a,b) and 0, 15, and 30% Sb calcined at 800 °C (Figure 5c,d) to study the elemental composition of the aerogel materials and to analyze the oxidation state of Sn and Sb. Survey scans between binding energies of 470 and 550 eV were made for all samples, along with high-resolution spectra (1000 scans) from 525 to 545 eV for the doped samples. The tin peaks corresponding to $3d_{3/2}$ and $3d_{5/2}$ electrons were found at binding energies of 495 and 488 eV, respectively, confirming the presence of Sn(IV) in the material regardless of calcination temperature.[51] No chlorine, nitrogen, or fluorine was detected in doped samples, suggesting that these byproducts had been either washed out in the gel aging/washing process or volatilized during the calcination step. Undoped samples showed a small peak for fluorine at both

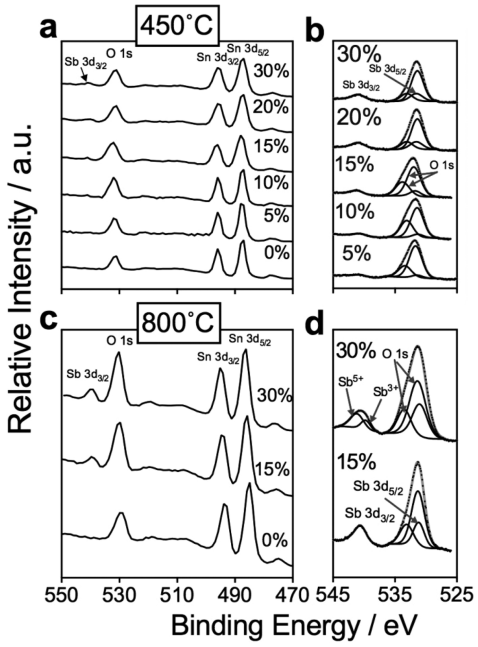

Figure 5. XPS spectra of undoped and Sb-doped SnO_2 and the respective high resolution spectra of the Sb 3d and O 1s peaks with fitted lines using CasaXPS software for samples calcined at 450 °C (a and b) and 800 °C (c and d). Each trace is labeled with the precursor % Sb.

calcination temperatures but no chlorine or nitrogen was detected.

The high-resolution scans allowed the quantification of Sb relative to Sn, and the resulting values are included in Table 2. The $3d_{3/2}$ peak of Sb at 541 eV was used because the $3d_{5/2}$ peak interferes with that of O 1s at a binding energy near 531 eV. For aerogels calcined at 450 °C, the measurement confirmed the presence of the dopant and the Sb:Sn ratio was consistently slightly more than half of its value in the precursor solution. Such incomplete incorporation of dopants is common in sol–gel processes.[52] Surprisingly, the 800 °C samples had higher Sb:Sn ratios, close to the precursor values. Because XPS is a surface-sensitive technique, we attribute this observation to the migration of antimony atoms toward the surface, as has been suggested by other reports.[53,54] Indeed, if many Sb atoms reside at interior grain boundaries following calcination at 450 °C, their migration to the surface may be triggered by the elimination of grain boundaries in the course of particle growth as the calcination temperature is increased.

It has been widely reported that the conductivity of ATO materials depends on an excess of Sb(V), which introduces donor states (electrons), with respect to Sb(III), which provides acceptor states (holes).[13,55] The resistivity of the material is therefore correlated to the concentration difference between the two oxidation states. While some reports[52,55] have found some conversion of Sb(V) to Sb(III) at high doping levels, our XPS high-resolution spectra (Figure 5b,d) showed that only Sb(V) was present, with the exception of a small amount of Sb(III) found in 30% Sb samples calcined at 800 °C. The $3d_{3/2}$ Sb peaks of all but one sample are found at 540.5 eV, which is attributed to Sb(V).[56,57] For the 30% Sb sample calcined at 800 °C, two $3d_{3/2}$ Sb peaks were observed at 540.7 and 539.4 eV, corresponding with values found elsewhere for Sb (V) and Sb(III), respectively.[56,58] An X-ray absorption finite structure (XANES) measurement study[36] found that Sb(III) is more prevalent for materials using Sb(III) in the precursor, with lower Sb(III) found when using Sb(V) in the precursor solution. This trend disappears and Sb(III) detected increases when the material is calcined at high temperatures, similar to our findings. These results support the supposition that the consistent decrease in resistivity is due to the additional electrons from Sb(V) in the conduction band. The deconvoluted O 1s curve exhibits two fitted peaks at about 533 and 531 eV, which suggests there are two oxygen types. The O 1s peak at 531 eV corresponds to the lattice oxygen atoms in SnO_2,[59,60] and the one at 533 eV to water and hydroxyl groups not part of the SnO_2 crystal structure.[61–64]

3.4. Electrical Properties. Electronic properties of bulk aerogels calcined at 450 °C for 30 min in air without any further treatment were characterized using four-point probe measurements. To the best of our knowledge, this is the first time such conductivity measurements have been made on uncompressed, nanoparticulate materials without a modification to the bulk structure, such as those made via the use of block copolymer methods to cast as films[15] or by pellitization of powders.[37,38,42,65–67] The networked structure of interconnected particles inherent to aerogels allowed current–voltage (I–V) measurements that are not feasible for powders that have not been pelletized. Figure 6 (top) summarizes the

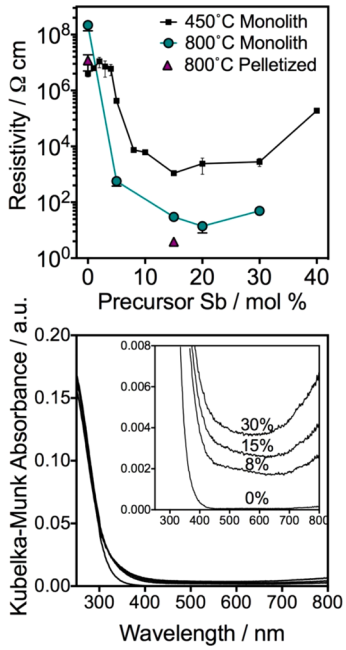

Figure 6. Resistivity plot of monolithic aerogel disks and pellets as a function of Sb precursor concentration and temperature (top) and Kubelka–Munk transform of UV–vis diffuse reflectance of doped and undoped SnO_2 calcined at 450 °C with an expanded view of the visible region in the inset (bottom).

resistivity of ATO monolithic aerogels at different doping concentrations calcined at 450 °C. The undoped samples exhibited a high resistivity of $\rho = 4 \times 10^6$ Ω·cm, which then dropped consistently to reach a minimum of $\rho = 1.1 \times 10^3$ Ω·cm at 15% Sb and then increased slightly at 20 and 30% Sb and more significantly at 40% Sb (based on the precursor Sb fraction). Comparable resistivities on the order of 10^3 Ω·cm[68] and 10^2 Ω·cm[42] have been reported for pelletized ITO materials calcined at 400 and 600 °C, respectively.

Measurements were also performed for aerogel monoliths containing 0, 5, 15, 20, and 30% Sb and calcined at 800 °C for 6 h. The results show a further 2-order-of-magnitude decrease in resistivity to 14 Ω·cm for the 20% Sb samples, and 1 order of magnitude increase to about 2×10^8 Ω·cm for the undoped samples (Figure 6, top). These results yield a 7-order-of-magnitude decrease in resistivity with 20% Sb doping. The reduction of the resistivity of these materials by high-temperature calcination can be explained by the increase in crystallite size from 3 to 9 nm (for the 15% Sb sample, for instance) and particle sintering, and the burning off of some carbon species left over from the synthesis process. These results are consistent with those reported by Nütz et al. with pelletized ATO nanoparticle (7 nm) materials calcined at 900 °C that exhibited resistivities of about 10 Ω·cm.[38] Calcination of the undoped SnO_2 aerogel at 800 °C greatly increased its crystallite size to 30 nm; it is unclear why its resistivity is not reduced as is that of the 15% Sb samples.

To compare the resistivities of the aerogels with those in the literature, we measured resistivities of pelletized undoped and 15% Sb-doped SnO_2 aerogels calcined at 800 °C for 6 h (Figure 6 top, triangles). Pelletization reduced the measured resistivities by about 1 order of magnitude compared to bulk aerogel samples, with the pelletized 15% Sb-doped sample reaching a resistivity as low as 3 Ω·cm. This is not surprising because the reduction of pore space and the increase of contact area between particles should decrease resistivity.

Compact ATO films have been reported to possess several orders of magnitude lower resistivity than these porous materials.[69] This can be explained by the nature of nanoparticulate grain boundary electron scattering,[9] which decreases electron mobility in the nanoparticle array. For crystallite sizes in the range of 3−4 nm, the number of grain boundaries is very large. Calcining the aerogel samples at 450 °C yielded both decreased resistivity and minimal shrinkage of the aerogel structure, both important properties for applications including making conducting thin films of aerogels without cracking or delamination.

3.5. Optical Properties. The optical absorbance for aerogel samples calcined at 450 °C was characterized by diffuse reflectance spectroscopy (Figure 6, bottom). It was found that undoped aerogels have negligible Kubelka−Munk absorbance in the visible range. With increased Sb content, the absorbance increased but overall remained low. The doped aerogels absorbed more in the longer wavelengths, resulting in the blue coloration of materials in Figure 1 (top). This trend is similar to those seen in reports of doped SnO_2 materials.[67] Our optical data do not indicate a significant shift in the bandgap due to Sb doping. The net effect of heavy doping can be small, as the Burnstein−Moss effect is offset by band tailing and other interactions.[70] For example, Benrabah et al.[71] measured a shift of less than 0.1 eV for Sb doping up to 10%.

4. CONCLUSIONS

Antimony doped tin oxide aerogels have been synthesized and characterized based on facile epoxide-assisted synthetic processing. In our sol−gel procedure, the addition of NH_4F to the precursor solution did not result in significant incorporation of F or reduction of resistivity, but it significantly reduced aerogel shrinkage during calcination. The use of $SbCl_5$ together with NH_4F resulted in Sb incorporation and a 3.5-order-of-magnitude reduction in resistivity to 1.1×10^3 Ω·cm for samples calcined at 450 °C at the optimal Sb:Sn precursor ratio of 15%. The Sb-doped materials exhibited low visible light absorbance. Calcining at 800 °C for 6 h yielded a further 2 orders of magnitude decrease in the monolithic aerogel resistivity to 30 Ω·cm, partly due to increased crystallite size. However, a trade-off exists as materials calcined at this temperature also yield low surface area and pore volume, which are desirable properties of aerogels. Sb-doped materials calcined at 450 °C yield a balance of increased conductivity and morphological traits typical of aerogels. The high surface area and open pore structure of these materials, along with their high conductivity and low absorbance, make them well suited to optoelectronic applications.

AUTHOR INFORMATION

Corresponding Author

*A. G. Agrios. E-mail: agrios@engr.uconn.edu. Tel: +1 860 486 1350.

Author Contributions

The paper was written through contributions of all authors. All authors have given approval to the final version of the paper.

Notes

The authors declare no competing financial interest.

ACKNOWLEDGMENTS

This material is based upon work supported by the National Science Foundation under Grant No. CBET-1332022. J.P.C.B. was also supported by NSF Grant No. DGE-0947869. The authors thank Guangliang Liu for the TEM image; the group of Dr. Steven Suib, in particular David Kriz, for fruitful discussions and help with diffuse reflectance measurements; Drs. Ali Gokirmak and Helena Silva, and Lhacene Adnane for use of and help with their four-probe measurement apparatus; Dr. Heng Zhang for XPS assistance. XPS was measured at the Institute of Material Science and XRD and SEM at the Center for Clean Energy Engineering, both at U. Connecticut.

ABBREVIATIONS

ATO, antimony-doped tin oxide
BET, Brunauer−Emmett−Teller
BJH, Barrett−Joyner−Halenda
DSC, dye-sensitized solar cell
FTO, fluorine-doped tin oxide
ITO, indium tin oxide
PPO, propylene oxide
SCD, supercritical drying
SEM, scanning electron microscopy
TCO, transparent conducting oxide
TEM, transmission electron microscopy
XANES, X-ray absorption finite structure
XPS, X-ray photoelectron spectroscopy
XRD, X-ray diffraction

REFERENCES

(1) Fukano, T.; Motohiro, T. Low-Temperature Growth of Highly Crystallized Transparent Conductive Fluorine-Doped Tin Oxide Films by Intermittent Spray Pyrolysis Deposition. *Sol. Energy Mater. Sol. Cells* **2004**, *82*, 567−575.

(2) Yang, Z.; Gao, S.; Li, T.; Liu, F.-Q.; Ren, Y.; Xu, T. Enhanced Electron Extraction from Template-Free 3D Nanoparticulate Transparent Conducting Oxide (TCO) Electrodes for Dye-Sensitized Solar Cells. *ACS Appl. Mater. Interfaces* **2012**, *4*, 4419−4427.

(3) Granqvist, C. G. Transparent Conductors as Solar Energy Materials: A Panoramic Review. *Sol. Energy Mater. Sol. Cells* **2007**, *91*, 1529−1598.
(4) Yin, Z.; Wang, Z.; Du, Y.; Qi, X.; Huang, Y.; Xue, C.; Zhang, H. Full Solution-Processed Synthesis of All Metal Oxide-based Tree-like Heterostructures on Fluorine-Doped Tin Oxide for Water Splitting. *Adv. Mater.* **2012**, *24*, 5374−5378.
(5) Liu, H.; Avrutin, v.; Izyumskaya, N.; Özgür, Ü.; Morkoç, H. Transparent Conducting Oxides for Electrode Applications in Light Emitting and Absorbing Devices. *Superlattices Microstruct.* **2010**, *48*, 458−484.
(6) Chaisitsak, S. Nanocrystalline SnO_2:F Thin Films for Liquid Petroleum Gas Sensors. *Sensors* **2011**, *11*, 7127−7140.
(7) Hamd, W.; Wu, Y. C.; Boulle, A.; Thune, E.; Guinebretière, R. Microstructural Study of SnO_2 Thin Layers Deposited on Sapphire by Sol−Gel Dip-Coating. *Thin Solid Films* **2009**, *518*, 1−5.
(8) Sheel, D. W.; Yates, H. M.; Evans, P.; Dagkaldiran, U.; Gordijn, A.; Finger, F.; Remes, Z.; Vanecek, M. Atmospheric Pressure Chemical Vapour Deposition of F Doped SnO_2 for Optimum Performance Solar Cells. *Thin Solid Films* **2009**, *517*, 3061−3065.
(9) Shanthi, E.; Dutta, V.; Banerjee, A.; Chopra, K. L. Electrical and Optical Properties of Undoped and Antimony-Doped Tin Oxide Films. *J. Appl. Phys.* **1980**, *51*, 6243−6251.
(10) Elangovan, E.; Ramamurthi, K. Optoelectronic Properties of Spray Deposited SnO_2:F Thin Films for Window Materials in Solar Cells. *J. Optoelectron. Adv. Mater.* **2003**, *5*, 45−54.
(11) Buonsanti, R.; Milliron, D. J. Chemistry of Doped Colloidal Nanocrystals. *Chem. Mater.* **2013**, *25*, 1305−1317.
(12) Wu, S.; Yuan, S.; Shi, L.; Zhao, Y.; Fang, J. Preparation, Characterization and Electrical Properties of Fluorine-Doped Tin Dioxide Nanocrystals. *J. Colloid Interface Sci.* **2010**, *346*, 12−16.
(13) Müller, V.; Rasp, M.; Štefanić, G.; Ba, J.; Günther, S.; Rathousky, J.; Niederberger, M.; Fattakhova-Rohlfing, D. Highly Conducting Nanosized Monodispersed Antimony-Doped Tin Oxide Particles Synthesized Via Nonaqueous Sol−Gel Procedure. *Chem. Mater.* **2009**, *21*, 5229−5236.
(14) Nütz, T.; Haase, M. Wet-Chemical Synthesis of Doped Nanoparticles: Optical Properties of Oxygen-Deficient and Antimony-Doped Colloidal SnO_2. *J. Phys. Chem. B* **2000**, *104*, 8430−8437.
(15) Müller, V.; Rasp, M.; Rathousky, J.; Schütz, B.; Niederberger, M.; Fattakhova-Rohlfing, D. Transparent Conducting Films of Antimony-Doped Tin Oxide with Uniform Mesostructure Assembled from Preformed Nanocrystals. *Small* **2010**, *6*, 633−637.
(16) Müller, V.; Rasp, M.; Štefanić, G.; Günther, S.; Rathousky, J.; Niederberger, M.; Fattakhova-Rohlfing, D. Antimony Doped Tin Oxide Nanoparticles and Their Assembly in Mesostructured Film. *Phys. Status Solidi C* **2011**, *8*, 1759−1763.
(17) Sanchez, C.; Boissière, C.; Grosso, D.; Laberty, C.; Nicole, L. Design, Synthesis, and Properties of Inorganic and Hybrid Thin Films Having Periodically Organized Nanoporosity. *Chem. Mater.* **2008**, *20*, 682−737.
(18) Fattakhova-Rohlfing, D.; Brezesinski, T.; Rathouský, J.; Feldhoff, A.; Oekermann, T.; Wark, M.; Smarsly, B. M. Transparent Conducting Films of Indium Tin Oxide with 3D Mesopore Architecture. *Adv. Mater.* **2006**, *18*, 2980−2983.
(19) Peng, Q.; Kalanyan, B.; Hoertz, P. G.; Miller, A.; Kim, D. H.; Hanson, K.; Alibabaei, L.; Liu, J.; Meyer, T. J.; Parsons, G. N.; Glass, J. T. Solution-Processed, Antimony-Doped Tin Oxide Colloid Films Enable High-Performance TiO_2 Photoanodes for Water Splitting. *Nano Lett.* **2013**, *13*, 1481−1488.
(20) Pierre, A. C.; Pajonk, G. M. Chemistry of Aerogels and Their Applications. *Chem. Rev.* **2002**, *102*, 4243−4266.
(21) Dorcheh, A. S.; Abbasi, M. H. Silica Aerogel; Synthesis, Properties and Characterization. *J. Mater. Process. Technol.* **2008**, *199*, 10−26.
(22) Pajonk, G. M.; Elaloui, E.; Achard, P.; Chevalier, B.; Chevalier, J.-L.; Durant, M. Physical Properties of Silica Gels and Aerogels Prepared with New Polymeric Precursors. *J. Non-Cryst. Solids* **1995**, *186*, 1−8.
(23) Gash, A. E.; Tillotson, T. M.; H, S. J.; Poco, J. F.; Hrubesh, L. W.; Simpson, R. L. Use of Epoxides in the Sol−Gel Synthesis of Porous Iron(III) Oxide Monoliths from Fe(III) Salts. *Chem. Mater.* **2001**, *13*, 999−1007.
(24) Gao, Y. P.; Sisk, C. N.; Hope-Weeks, L. J. A Sol−Gel Route to Synthesize Monolithic Zinc Oxide Aerogels. *Chem. Mater.* **2007**, *19*, 6007−6011.
(25) Baumann, T. F.; Kucheyev, S. O.; Gash, A. E.; Satcher, J. H. Facile Synthesis of a Crystalline, High-Surface-Area SnO_2 Aerogel. *Adv. Mater.* **2005**, *17*, 1546−1548.
(26) Hamann, T. W.; Martinson, A. B. F.; Elam, J. W.; Pellin, M. J.; Hupp, J. T. Atomic Layer Deposition of TiO_2 on Aerogel Templates: New Photoanodes for Dye-Sensitized Solar Cells. *J. Phys. Chem. C* **2008**, *112*, 10303−10307.
(27) Hamann, T. W.; Martinson, A. B. F.; Elam, J. W.; Pellin, M. J.; Hupp, J. T. Aerogel Templated ZnO Dye-Sensitized Solar Cells. *Adv. Mater.* **2008**, *20*, 1560−1564.
(28) Correa Baena, J. P.; Agrios, A. G. Antimony-Doped Tin Oxide Aerogels as Porous Electron Collectors for Dye-Sensitized Solar Cells. *J. Phys. Chem. C* **2014**, *118*, 17028−17035.
(29) Kawashima, T.; Matsui, H. New Transparent Conductive Films: FTO Coated ITO. *Thin Solid Films* **2003**, *445*, 241−244.
(30) Patterson, A. L. The Scherrer Formula for X-Ray Particle Size Determination. *Phys. Rev.* **1939**, *56*, 978−982.
(31) Schroder, D. K. *Semiconductor Material and Device Characterization*, 2nd ed.; Wiley-Interscience: New York, NY, 2006; Chapter 1, pp 1−20.
(32) Pope, E. J. A.; Mackenzie, J. D. Sol-Gel Processing of Silica. *J. Non-Cryst. Solids* **1986**, *87*, 185−198.
(33) Mrowiec-Białoń, J.; Pająk, L.; Jarzębski, A. B.; Lachowski, A. I.; Malinowski, J. J. Morphology of Silica Aerogels Obtained from the Process Catalyzed by NH_4F and NH_4OH. *Langmuir* **1997**, *13*, 6310−6314.
(34) Boschloo, G.; Fitzmaurice, D. Spectroelectrochemistry of Highly Doped Nanostructured Tin Dioxide Electrodes. *J. Phys. Chem. B* **1999**, *103*, 3093−3098.
(35) Kim, D.-W.; Kim, D.-S.; Kim, Y.-G.; Kim, Y.-C.; Oh, S.-G. Preparation of Hard Agglomerates Free and Weakly Agglomerated Antimony Doped Tin Oxide (ATO) Nanoparticles by Coprecipitation Reaction in Methanol Reaction Medium. *Mater. Chem. Phys.* **2006**, *97*, 452−457.
(36) Rockenberger, J.; zum Felde, U.; Tischer, M.; Tröger, L.; Haase, M.; Weller, H. Near Edge X-ray Absorption Fine Structure Measurements (XANES) and Extended X-ray Absorption Fine Structure Measurements (EXAFS) of the Valence State and Coordination of Antimony in Doped Nanocrystalline SnO_2. *J. Chem. Phys.* **2000**, *112*, 4296−4304.
(37) Naghavi, N.; Marcel, C.; Dupont, L.; Leriche, J.-B.; Tarascon, J.-M. On the Electrochromic Properties of Antimony−Tin Oxide Thin Films Deposited by Pulsed Laser Deposition. *Solid State Ionics* **2003**, *156*, 463−474.
(38) Nütz, T.; zum Felde, U.; Haase, M. Wet-Chemical Synthesis of Doped Nanoparticles: Blue-Colored Colloids of N-Doped SnO_2:Sb. *J. Chem. Phys.* **1999**, *110*, 12142−12150.
(39) Gregg, S. J.; Sing, K. S. W. *Adsorption, Surface Area and Porosity*, 2nd ed.; Academic Press: London, 1982.
(40) Li, T. C.; Fabregat-Santiago, F.; Farha, O. K.; Spokoyny, A. M.; Raga, S. R.; Bisquert, J.; Mirkin, C. A.; Marks, T. J.; Hupp, J. T. SiO_2 Aerogel Templated, Porous TiO_2 Photoanodes for Enhanced Performance in Dye-Sensitized Solar Cells Containing a Ni(III)/(IV) Bis(dicarbollide) Shuttle. *J. Phys. Chem. C* **2011**, *115*, 11257−11264.
(41) Suh, D. J.; Park, T.-J. Sol−Gel Strategies for Pore Size Control of High-Surface-Area Transition-Metal Oxide Aerogels. *Chem. Mater.* **1996**, *8*, 509−513.
(42) Mercera, P. D. L.; Van Ommen, J. G.; Doesburg, E. B. M.; Burggraaf, A. J.; Ross, J. R. H. Zirconia as a Support for Catalysts: Evolution of the Texture and Structure on Calcination in Air. *Appl. Catal.* **1990**, *57*, 127−148.

(43) Davis, M.; Zhang, K.; Wang, S.; Hope-Weeks, L. J. Enhanced Electrical Conductivity in Mesoporous 3D Indium-Tin Oxide Materials. *J. Mater. Chem.* **2012**, *22*, 20163−20165.
(44) Chandiran, A. K.; Sauvage, F. d. r.; Casas-Cabanas, M.; Comte, P.; Zakeeruddin, S. M.; Graetzel, M. Doping a TiO_2 Photoanode with Nb^{5+} to Enhance Transparency and Charge Collection Efficiency in Dye-Sensitized Solar Cells. *J. Phys. Chem. C* **2010**, *114*, 15849−15856.
(45) Lee, K.-T.; Lu, S.-Y. Porous FTO Thin Layers Created with a Facile One-Step Sn^{4+}-based Anodic Deposition Process and Their Potential Applications in Ion Sensing. *J. Mater. Chem.* **2012**, *22*, 16259−16268.
(46) Trotochaud, L.; Boettcher, S. W. Synthesis of Rutile-Phase $Sn_xTi_{1-x}O_2$ Solid-Solution and $(SnO_2)_x/(TiO_2)_{1-x}$ Core/Shell Nanoparticles with Tunable Lattice Constants and Controlled Morphologies. *Chem. Mater.* **2011**, *23*, 4920−4930.
(47) Liu, T. J.; Jin, Z. G.; Feng, L. R.; Wang, T. Conducting Antimony-Doped Tin Oxide Films Derived from Stannous Oxalate by Aqueous Sol−Gel Method. *Appl. Surf. Sci.* **2008**, *254*, 6547−6553.
(48) Goebbert, C.; A Aegerter, M.; Burgard, D.; Nass, R.; Schmidt, H. Ultrafiltration Conducting Membranes and Coatings from Redispersable, Nanoscaled, Crystalline SnO_2:Sb Particles. *J. Mater. Chem.* **1999**, *9*, 253−258.
(49) Lin, Y.-J.; Wu, C.-J. The Properties of Antimony-Doped Tin Oxide Thin Films from the Sol-Gel Process. *Surf. Coat. Technol.* **1997**, *88*, 239−247.
(50) Woo, D. C.; Koo, C. Y.; Ma, H. C.; Lee, H. Y. Characterization of Sol-Gel Derived Antimony-Doped Tin Oxide Thin Films for Transparent Conductive Oxide Application. *Trans. Electr. Electron. Mater.* **2012**, *13*, 241−244.
(51) Stranick, M. A.; Moskwa, A. SnO_2 by XPS. *Surf. Sci. Spectra* **1993**, *2*, 50−54.
(52) Terrier, C.; Chatelon, J. P.; Roger, J. A.; Berjoan, R.; Dubois, C. Analysis of Antimony Doping in Tin Oxide Thin Films Obtained by the Sol-Gel Method. *J. Sol-Gel Sci. Technol.* **1997**, *10*, 75−81.
(53) Berry, F. J. A Mössbauer Investigation of the Formation and Surface Composition of Tin-Antimony Oxide Catalysts. *J. Catal.* **1982**, *73*, 349−356.
(54) Van Bommel, M. J.; Groen, W. A.; Van Hal, H. A. M.; Keur, W. C.; Bernards, T. N. M. The Electrical and Optical Properties of Thin Layers of Nano-Sized Antimony Doped Tinoxide Particles. *J. Mater. Sci.* **1999**, *34*, 4803−4809.
(55) Terrier, C.; Chatelon, J. P.; Berjoan, R.; Roger, J. A. Sb-Doped SnO_2 Transparent Conducting Oxide from the Sol-Gel Dip-Coating Technique. *Thin Solid Films* **1995**, *263*, 37−41.
(56) Izquierdo, R.; Sacher, E.; Yelon, A. X-ray Photoelectron Spectra of Antimony Oxides. *Appl. Surf. Sci.* **1989**, *40*, 175−177.
(57) Jianqi, W.; Daming, F.; Wenhui, W.; Minxiu, Z.; Yiz, L. An Investigation of the Flame Retardation Mechanism of Polypropylene Containing a Chlorine Flame Retardant System by XPS(ESCA). *Polym. Degrad. Stab.* **1991**, *31*, 129−140.
(58) Benvenutti, E. V.; Gushikem, Y.; Vasquez, A.; de Castro, S. C.; Zaldivar, G. A. P. X-ray Photoelectron Spectroscopy and Mössbauer Spectroscopy Study of Iron(III) and Antimony(V) Oxides Grafted onto a Silica Gel Surface. *J. Chem. Soc., Chem. Commun.* **1991**, 1325−1327.
(59) Shiratsuchi, R.; Hongo, K.; Nogami, G.; Ishimaru, S. Reduction of CO_2 on Fluorine-Doped SnO_2 Thin-Film Electrodes. *J. Electrochem. Soc.* **1992**, *139*, 2544.
(60) Badrinarayanan, S.; Mandale, A. B.; Gunjikar, V. G.; Sinha, A. P. B. Mechanism of High-Temperature Oxidation of Tin Selenide. *J. Mater. Sci.* **1986**, *21*, 3333−3338.
(61) Nefedov, V. I.; Gati, D.; Dzhurinskii, B. F.; Sergushin, N. P.; Salyn, Y. V. The X-ray Electronic Studies of Oxides of Certain Elements. *Zh. Neorg. Khim.* **1975**, *20*, 2307.
(62) Wagner, C. D.; Zatko, D. A.; Raymond, R. H. Use of the Oxygen Kll Auger Lines in Identification of Surface Chemical States by Electron Spectroscopy for Chemical Analysis. *Anal. Chem.* **1980**, *52*, 1445−1451.
(63) Pan, X. Q.; Fu, L. Oxidation and Phase Transitions of Epitaxial Tin Oxide Thin Films on $(\bar{1}012)$ Sapphire. *J. Appl. Phys.* **2001**, *89*, 6048−6055.
(64) Zhao, Q.; Xie, Y.; Dong, T.; Zhang, Z. Oxidation−Crystallization Process of Colloids: An Effective Approach for the Morphology Controllable Synthesis of SnO_2 Hollow Spheres and Rod Bundles. *J. Phys. Chem. C* **2007**, *111*, 11598−11603.
(65) Rolison, D. R.; Dunn, B. Electrically Conductive Oxide Aerogels: New Materials in Electrochemistry. *J. Mater. Chem.* **2001**, *11*, 963−980.
(66) Jeon, H.-J.; Jeon, M.-K.; Kang, M.; Lee, S.-G.; Lee, Y.-L.; Hong, Y.-K.; Choi, B.-H. Synthesis and Characterization of Antimony-Doped Tin Oxide (ATO) with Nanometer-Sized Particles and Their Conductivities. *Mater. Lett.* **2005**, *59*, 1801−1810.
(67) Volosin, A. M.; Sharma, S.; Traverse, C.; Newman, N.; Seo, D.-K. One-Pot Synthesis of Highly Mesoporous Antimony-Doped Tin Oxide from Interpenetrating Inorganic/Organic Networks. *J. Mater. Chem.* **2011**, *21*, 13232−13240.
(68) Emons, T. T.; Li, J.; Nazar, L. F. Synthesis and Characterization of Mesoporous Indium Tin Oxide Possessing an Electronically Conductive Framework. *J. Am. Chem. Soc.* **2002**, *124*, 8516−8517.
(69) Kim, K.-S.; Yoon, S.-Y.; Lee, W.-J.; Ho Kim, K. Surface Morphologies and Electrical Properties of Antimony-Doped Tin Oxide Films Deposited by Plasma-Enhanced Chemical Vapor Deposition. *Surf. Coat. Technol.* **2001**, *138*, 229−236.
(70) Lin, Y.-Y.; Lee, H.-Y.; Ku, C.-S.; Chou, L.-W.; Wu, A. T. Bandgap Narrowing in High Dopant Tin Oxide Degenerate Thin Film Produced by Atmosphere Pressure Chemical Vapor Deposition. *Appl. Phys. Lett.* **2013**, *102*, 111912.
(71) Benrabah, B.; Bouaza, A.; Hamzaoui, S.; Dehbi, A. Sol-Gel Preparation and Characterization of Antimony Doped Tin Oxide (ATO) Powders and Thin Films. *Eur. Phys. J.: Appl. Phys.* **2009**, *48*, 30301.